Matter

CellPress

Article

Designing transparent conductors using forbidden optical transitions

As scientists search for new materials to enable devices like solar cells, finding excellent p-type transparent conductors ("p-type TCs") is particularly challenging. The presence of "forbidden optical transitions" enhances transparency in n-type TCs, but searches for p-type TCs usually overlook this. Here, optical properties across ~18,000 semiconductors demonstrate forbidden transitions in over half. Computationally screening this data yields new p-type TC candidates with forbidden transitions such as $BeSiP_2$ and BAs and inspires future experimental work to test these predictions.

Rachel Woods-Robinson, Yihuang Xiong, Jimmy-Xuan Shen, ..., Alex M. Ganose, Geoffroy Hautier, Kristin A. Persson

rwoodsrobinson@berkeley.edu

Highlights

In some cases, band edge is optically forbidden so absorption onsets above the gap

Across 18,000 materials, half have forbidden optical transitions at band edge

Localized states at band edges can lead to these forbidden transitions

New transparent conductors with forbidden transitions are identified ($BeSiP_2$, BAs)

Benchmark

First qualification/assessment of material properties and/or performance

Woods-Robinson et al., Matter 6, 3021–3039
September 6, 2023 © 2023 Published by Elsevier Inc.
https://doi.org/10.1016/j.matt.2023.06.043

Matter

CellPress

Article

Designing transparent conductors using forbidden optical transitions

Rachel Woods-Robinson,[1,2,8,*] Yihuang Xiong,[3] Jimmy-Xuan Shen,[4] Nicholas Winner,[1,6] Matthew K. Horton,[1] Mark Asta,[1,6] Alex M. Ganose,[5] Geoffroy Hautier,[3] and Kristin A. Persson[6,7]

SUMMARY

Many semiconductors present weak or forbidden transitions at their fundamental band gaps, inducing a widened region of transparency. This occurs in high-performing n-type transparent conductors (TCs) such as Sn-doped In_2O_3 (ITO); however, thus far, the presence of forbidden transitions has been neglected in the search for new p-type TCs. To address this, we first compute high-throughput absorption spectra across ∼18,000 semiconductors, showing that over half exhibit forbidden or weak optical transitions at their band edges. Next, we demonstrate that compounds with highly localized band-edge states are more likely to present forbidden transitions. Lastly, we search this set for p-type and n-type TCs with forbidden transitions and, by performing defect calculations, propose unexplored TC candidates such as ambipolar $BeSiP_2$, p-type wurtzite BAs, and n-type Ba_2InGaO_5, among others. We share our dataset and recommend that future screenings for optical properties consider the impact of forbidden transitions.

INTRODUCTION

It is often assumed in semiconductors that a strong absorption onset occurs at the direct fundamental band gap. This is indeed the case for many materials; however, some materials have forbidden transitions at their band edges such that the onset of their absorption edge occurs at higher energies than their direct gap. Four scenarios of absorption in semiconductors are depicted schematically in Figure 1, following the optical-type (OT) classification as outlined by Yu and Zunger[1] for four hypothetical materials with similar band structures. In OT1, the fundamental band gap E_G is direct and allowed ("da"); in OT2, E_G is direct but forbidden ("df"); in OT3, E_G is indirect and the direct gap is allowed ("ia"); and in OT4, E_G is indirect and the direct gap is forbidden ("if").

The presence of forbidden optical transitions can be detrimental in certain applications (e.g., LEDs, solar cell absorbers); however, for others, it may present a useful design criteria. In this study, we focus on transparent conductors (TCs)—materials combining wide optical transparency with high mobility and doping—which require weak absorption within a given range of wavelengths (usually within the visible) such that forbidden transitions could be advantageous to increase transparency. In fact, many of the high-performing, commercially available n-type transparent conducting oxides (TCOs) have dipole forbidden transitions at their band edges that induce this behavior. A notable example occurs in the most common TCO, n-type Sn-doped In_2O_3 (ITO), with weak absorption in the upper-most 0.8 eV of the valence band (VB), allowing for an increased transparency in addition to the increase from the

PROGRESS AND POTENTIAL

Scientists have been actively searching for new materials that are both conductive and highly transparent to visible light, which can enable advances in optoelectronics, solar cells, and display technologies. However, finding suitable materials with excellent transparency and p-type conductivity ("p-type transparent conductors," or "p-type TCs") has proven to be a particular challenge. Although the best-performing n-type TCs achieve transparency partly due to a special property—the presence of forbidden optical transitions at their band edges—searches for p-type TCs usually do not account for this property. Here, the presence of forbidden transitions and their impact on optical properties is explored across tens of thousands of semiconductors. From this set, new p-type TC candidates with forbidden transitions are identified. This study paves the way for future synthesis of predicted TCs, with the ultimate goal of incorporation into next-generation energy technologies.

Burstein-Moss effect.[3] Other wide-gap oxide materials with reported forbidden transitions include SnO_2 and F-doped SnO_2 (FTO)[4,5]; spinels $SnZn_2O_4$, $SnCd_2O_4$, and $CdIn_2O_4$[6]; Tl_2O_3[7]; and TiO_2.[8] Additionally, dipole-forbidden transitions have been reported in Cu-based p-type TCs including delafossites $CuAlO_2$, $CuGaO_2$, and $CuInO_2$, as well as cuprite Cu_2O.[9]

Meanwhile, it is of considerable interest to identify new high-performing p-type TC for applications in photovoltaics and beyond. Over the past decade, high-throughput screening studies have proposed several n-type or p-type TC candidates such as $ZnSb_2O_6$, ZrOS, BP, Ba_2BiTaO_6, and CaTe.[10–14] Experimental confirmation of promising properties has been demonstrated in some of those computationally identified materials such as the p-type Ba_2BiTaO_6 and the n-type $ZnSb_2O_6$,[12,15] but still, no predicted p-type TC has experimentally confirmed properties on par with n-type ITO. Most high-throughput screenings for TCs to date assume a wide electronic band gap or a direct band gap as a proxy for transparency.[10,13,16–19] This assumption does not consider whether associated optical transitions are actually allowed or whether they are strong and thus overlook materials with a small fundamental band gap but a wide absorption edge, which could enable optical transparency. We note that several screenings for solar absorbers have explicitly considered forbidden transitions,[1,20,21] excluding materials with forbidden edges to design for a sharp absorption onset; in contrast, a screening for TCs would include such materials.

Therefore, in this work, we leverage forbidden optical transitions at band edges (referred to hereafter as simply "forbidden transitions") to improve high-throughput searches for TCs. First, we benchmark and compute optical absorption edges for ~18,000 inorganic compounds in the Materials Project (MP) database and classify OTs across the MP to assess whether fundamental gaps are optically allowed or forbidden. We show that over half of the selected semiconductors in the MP exhibit a weak absorption edge and that, in special cases involving transitions between localized states, the presence of forbidden transitions can be explained by orbital character. With these data, we introduce a series of high-throughput descriptors for p-type TCs to estimate the direct allowed band gap (often referred to in the literature as the "optical gap"), the absorption edge onset, and the average absorption spectra in the visible spectrum. Using these descriptors, we perform a high-throughput screening (as outlined in Figure 2) for promising p-type and n-type TCs with disperse band edges that may be transparent in the visible regime. Such compounds have low fundamental band gaps and therefore may have previously been overlooked. To assess dopability and mobility for materials with good computed optical properties, we perform defect formation energy calculations and compute transport properties for the most promising candidates. We highlight some ambipolar TC candidates including $BeSiP_2$, p-type TC candidates including wurtzite BAs, and n-type TC candidates including barium indium gallium oxide (Ba_2InGaO_5) and share our data for further exploration.

RESULTS

Forbidden or weak transitions are common

As a result of the pre-screening, we obtain a dataset of ~18,000 semiconductor compounds for which optical absorption spectra and descriptors are assembled. Statistics and corresponding descriptors are summarized in Figure 3, grouped by OT. We first assess the distribution of OTs and forbidden optical transitions across the set. To our knowledge, this has not been assessed across known semiconductor materials

[1]Materials Sciences Division, Lawrence Berkeley National Laboratory, Berkeley, CA, USA
[2]Applied Science and Technology Graduate Group, University of California at Berkeley, Berkeley, CA, USA
[3]Thayer School of Engineering, Dartmouth College, 14 Engineering Dr., Hanover, NH, USA
[4]Lawrence Livermore National Laboratory, Livermore, CA, USA
[5]Department of Chemistry, Molecular Sciences Research Hub, White City Campus, Imperial College London, Wood Lane, London, UK
[6]Department of Materials Science and Engineering, University of California at Berkeley, Berkeley, CA, USA
[7]Molecular Foundry Division, Lawrence Berkeley National Laboratory, Berkeley, CA, USA
[8]Lead contact
*Correspondence: rwoodsrobinson@berkeley.edu
https://doi.org/10.1016/j.matt.2023.06.043

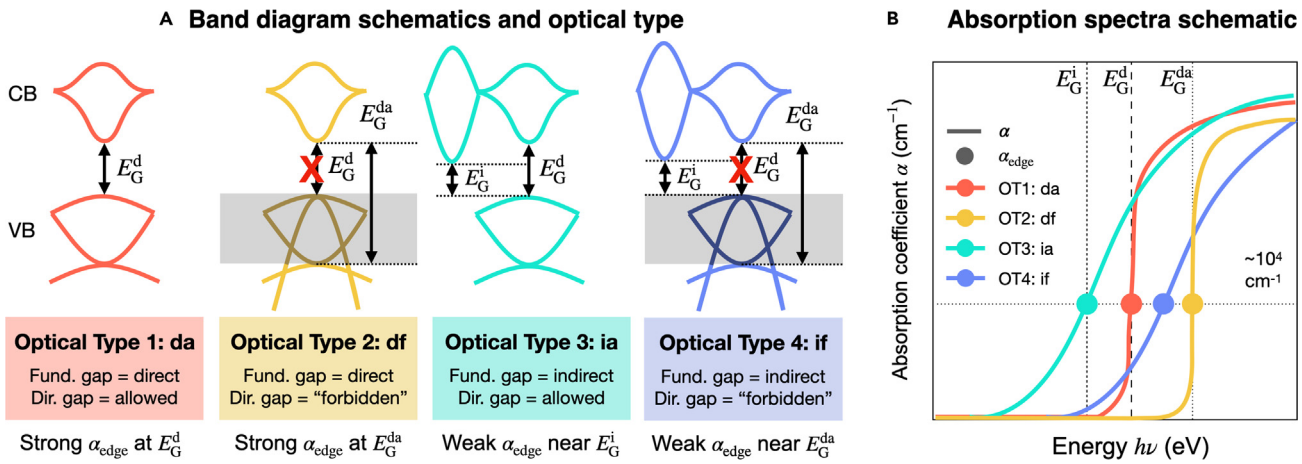

Figure 1. Band diagram and absorption schematics for semiconductors

(A and B) (A) Band schematics and (B) cartoon of the resulting absorption spectra of the four optical types (OTs) in semiconductor materials. Band schematics on the left are inspired by Yu and Zunger.[1] The gray regions in OT2 and OT4 correspond to the forbidden region where transitions do not occur. "Fund. gap" stands for fundamental electronic band gap, and "dir. gap" stands for direct band gap. The absorption schematic in (B) is intended as one possible configuration for hypothetical simplified materials but is derived from data from this study (see supplemental information); in real materials, features of the absorption spectra ultimately depend on multiple material properties. For schematic purposes, absorption spectra of indirect materials (OT3 and OT4) are broadened for $\alpha < 10^4$ cm^{-3} to reflect features due to phonon absorption[2]; however, phonon absorption is not computed in this study's high-throughput workflow.

except for the several hundred from Fabini et al.[21] Figure 3A plots a histogram of the descriptor "forbidden energy difference" Δ^d, defined as

$$\Delta^d = E_G^{da} - E_G^d, \qquad \text{(Equation 1)}$$

where the direct allowed band gap, E_G^{da}, is defined as the energy at which dipole transition matrix elements become significant (adopting what constitutes as "significant" from the literature[21]; see supplemental information). Here, properties from Purdue-Berke-Ernzerhof (PBE) calculations are reported. We demonstrate that nearly 50% of compounds have forbidden transitions (i.e., $\Delta^d > 0$ eV) at the band edges. A strong impact from forbidden compounds is observed in a large subset of compounds show a strong impact: ~18% with $\Delta^d > 0.2$ eV and 7% with $\Delta^d > 0.5$ eV. It is observed that OT3 (indirect gap, allowed direct transition) is the most common OT, followed closely by OT4 (indirect fundamental gap, forbidden direct transition).

Figure 3B reports the distribution of the "edge energy difference" Δ^d_{edge}, defined as

$$\Delta^d_{edge} = E_{edge} - E_G^d, \qquad \text{(Equation 2)}$$

where the absorption edge energy (E_{edge}) is defined as the energy at which the independent-particle approximation (IPA) absorption coefficient (computed with PBE) exceeds 10^4 cm^{-1} (see supplemental information). Some materials may have transitions at the band edges that are "allowed" but are only weakly absorbing; in these cases, E_{edge} can provide a better metric than E_G^{da} for where the strong edge onset actually occurs. For example, in In_2O_3 (dashed lines), our computed Δ^d_{edge} of 0.68 eV corresponds better to the literature-reported Δ^d than our computed PBE Δ^d of 0.22 eV. Third, in Figure 3C, we plot the distribution of the average absorption coefficient in the visible regime, $\overline{\alpha}_{vis}$, defined as

$$\overline{\alpha}_{vis} = \int_{\nu_{vis}^{min}}^{\nu_{vis}^{max}} \alpha(h\nu), \qquad \text{(Equation 3)}$$

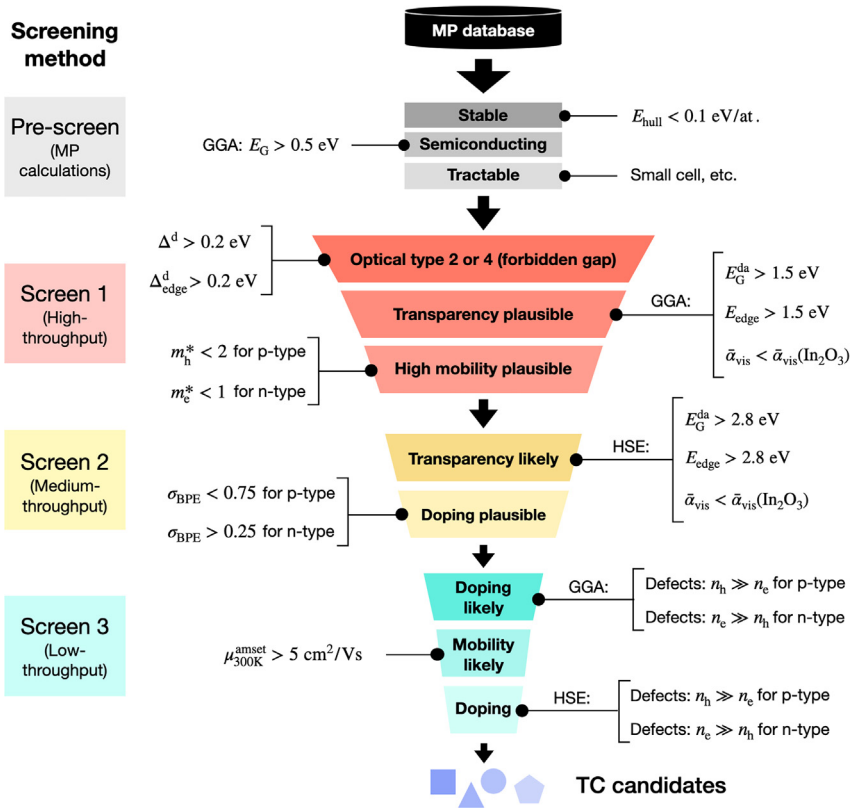

Figure 2. Screening method for TCs with forbidden transitions

The screening method for TCs pursued in this article, focusing on compounds from the MP database with forbidden optical transitions. The targeted property is listed in the screen, and the descriptor and cutoff value are given on the right-hand side. Descriptors with multiple options listed indicate that one or more of the criteria must be met (e.g., $\Delta^d > 0.2$ eV or $\Delta^d_{edge} > 0.2$ eV). Descriptors are computed with both PBE (for screen 1) and HSE06 (for screen 2) functionals and are described in more detail in the article.

i.e., the integral of the absorption spectra across the visible regime. Since the PBE Kohn-Sham gap underestimates the fundamental band gap, we define the limits of the integral for PBE calculations using an empirical gap correction from Morales et al. (see supplemental information).[22] It is observed that in more than 50% of compounds, $\bar{\alpha}_{vis}$ is less than that of In_2O_3. Of interest to this study is the set of compounds with a significantly widened absorption edge due to forbidden transitions and correspondingly low absorption coefficients. In particular, we are interested in materials in which forbidden transitions raise the absorption edge outside of the visible spectrum and lead to optical transparency. However, we note that this dataset may be valuable for other investigations as well.

Underlying chemical trends

Forbidden and weak optical transitions in semiconductors can arise from a variety of physical, structural, and chemical phenomena. Inversion symmetry at the band extrema can induce parity forbidden dipole transitions,[23] and a series of selection rules determine whether transitions can occur between states of different irreducible representation. Parity-forbidden transitions are invoked, e.g., for In_2O_3, among other materials, to explain in part why experimental optical band gaps exceed the fundamental gap. According to Fermi's golden rule, if symmetry allows, transitions between localized states composed of similar chemical orbitals (i.e., with significant

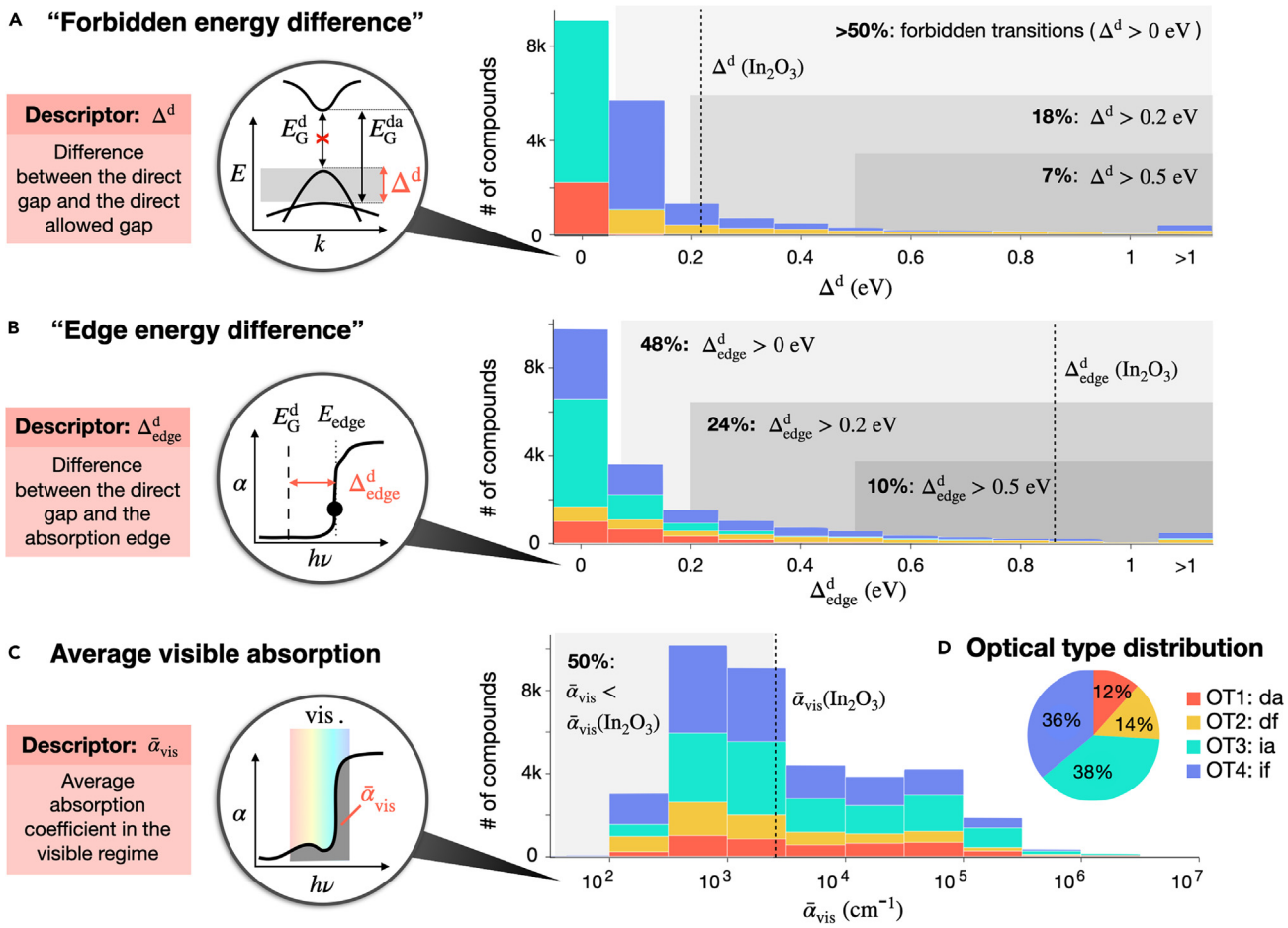

Figure 3. Statistic distribution of optical screening descriptors

(A–C) (Left) Schematics highlighting new optical screening descriptors: (A) "forbidden energy difference" (Δ^d), (B) edge energy difference (Δ^d_{edge}), and (C) average absorption in the visible regime ($\bar{\alpha}_{vis}$). (Right) Histograms of these three optical descriptors are reported across the set of 18,000 semiconductors. Corresponding values for In_2O_3, the best performing n-type TC, are denoted for reference.

(D) OT distribution, showing over half of this set has a forbidden direct optical transition, 18% exhibit Δ^d >0.2 eV, and 7% exhibit Δ^d >0.5 eV.

$\langle\psi_i|r|\psi_f\rangle$, which scales with orbital overlap $\langle\psi_i|\psi_f\rangle$) have weak dipole transition matrix elements.[23] However, due to the delocalized nature of wavefunctions in solids, understanding the mechanisms behind forbidden and allowed transitions is less straightforward in semiconductors than in molecules with discrete, localized states.

Here, we explore whether the nature of forbidden transitions between the direct band edges can be correlated with two simple orbital-based descriptors, described in Figure 4.

(1) "Inverse participation ratio" of the direct VB maximum (VBM) and conduction band minimum (CBM) states, t^d_{IPR}: we consider the inverse participation ratio (IPR) across all compounds as a proxy for localization of states at the band edges (a high IPR indicates strong localization).[24–27] As shown in Figure 4A, "D" indicates a delocalized state and "L" indicates a localized state, and values of descriptor t^d_{IPR} are assigned as shown in the call-out circle (e.g., t^d_{IPR} = "L → L" indicates a transition from a strongly localized VBM to a strongly localized CBM).

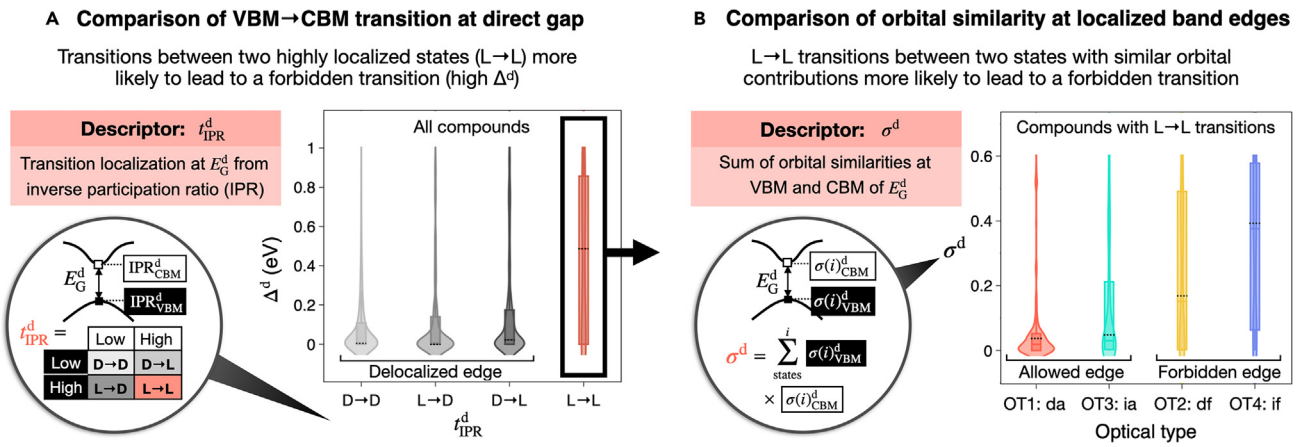

Figure 4. Statistical distribution of oribital descriptors

(A and B) A schematic of band-edge orbital descriptors and violin plots correlating each descriptor to the forbidden transitions dataset for (A) t^{d}_{IPR}, the transition localization at the VBM and CBM from the inverse participation ratio (IPR), and (B) $\Sigma\sigma^{d}$, the orbital similarity of the VBM and CBM states at E^{d}_{G}. In (A), "D" indicates a delocalized state, and "L" indicates a localized state, and the scenario in which there are transitions from a highly localized state at the VBM to another highly localized state at the CBM (L → L) is highlighted. In (B), only compounds with L → L are plotted, and the violin plot shows the distribution of $\Sigma\sigma^{d}$ across different OTs (note that OT2 and OT4 indicate forbidden transitions, i.e., $\Delta^{d} > 0$ eV) In both violin plots, mean values of each distribution are reported with dashed black lines.

(2) "Orbital similarity" of the direct VBM and CBM states, σ^{d}: for each compound, we consider the dominant contributors to the density of states at the direct VBM and CBM, $\sigma(l,m)^{d}$ (l is the angular momentum quantum number s, p, d, or f for each element, and m is magnetic quantum number; see supplemental information for details). With these data, we compute a descriptor σ^{d} (i.e., $\langle\psi_i|r|\psi_f\rangle$) to describe the similarity of CB-edge and VB-edge orbital contributions. This is depicted in the call-out circle in Figure 4B as

$$\sigma^{d} = \sum_{l,m} \sigma(l,m)^{d}_{VBM}\sigma(l,m)^{d}_{CBM} \qquad \text{(Equation 4)}$$

We will refer to this descriptor as "orbital similarity" in this article.

Basic trends between these descriptors and the forbidden nature of the gap are summarized in Figure 4. In the violin plot in Figure 4A, it is shown that in compounds in which states at both band edges are delocalized (D → D), the forbidden energy difference (Δ^{d}) is low, with a mean close to zero. In compounds where at least one band edge is delocalized (D → L and L → D), the average Δ^{d} increases slightly. However, compounds where both edges are highly localized (L → L) are significantly more likely to have wide forbidden transitions; the average Δ^{d} across such compounds is ~0.5 eV, and quartiles range from 0.1 to 0.6 eV. Therefore, transitions between two highly localized states are likely to lead to a forbidden transition.

To inspect cases with localized transitions in more detail, we compute the orbital similarity σ^{d} for the L → L subset from Figure 4A and report the distribution of σ^{d} across the four OTs in the violin plot in Figure 4B. It is observed that, systematically, compounds with allowed edges (OT1 and OT3) have significantly decreased orbital similarity than compounds with forbidden edges (OT2 and OT4). This is consistent with Fermi's golden rule: low transition dipole matrix elements (i.e., forbidden or weak transitions) should occur between localized states with similar

orbital contributions. We note that a weaker trend occurs when σ^d is plotted across all compounds (see supplemental information), mostly likely because the selection rules from Fermi's golden rule break down in transitions between delocalized states.

Therefore, in cases with highly localized band edges, σ^d is a useful predictor for the origin of forbidden transitions. However, these L → L cases are only a small subset (~10%) of compounds in which we observe forbidden transitions. There are likely other factors that contribute, for example, due to the delocalized or hybridized nature of edge states. Ultimately, due to the relatively cheap computational cost of high-throughput IPA calculations and the variety of mechanisms contributing to optical transition matrix elements, we recommend further density functional theory (DFT) calculations at this stage to determine whether transitions are allowed or forbidden.

Screening for TCs with forbidden transitions

Using this dataset, we perform a high-throughput screening for TCs with forbidden optical transitions at the band edges, which may have been excluded from previous screenings. We assess candidates for both p-type and n-type TCs. Our basic screening methodology is depicted in Figure 2A. We note that the pre-screening steps restrict compounds to those with E_{hull} < 0.1 eV/atom as a proxy for stability and to those with 12 or fewer symmetrically equivalent sites to allow for subsequent hybrid and defect calculations.

Screen 1: High-throughput absorption calculations

In screen 1, we filter compounds based on high-throughput PBE optical absorption calculations and corresponding effective masses at the band edges, as shown in the red-colored screening steps of Figure 2A. Rather than considering the fundamental band gap (E_G) or the direct band gap (E_G^d), as done in previous screenings for p-type TCs,[10–14,16–19] materials are filtered by either their direct allowed gap (E_G^{da}), the onset of the absorption edge (E_{edge}), or the average absorption coefficient in the visible regime ($\overline{\alpha}_{vis}$). Schematics of these descriptors are depicted in Figure 2B. We also prioritize compounds with large Δ^d or Δ^d_{edge}, which indicate whether there is a strong presence of optically forbidden transitions at the band edges that could lead to a widening of the absorption edge.

In Figures 5A and 5B, the hole and electron effective mass (m_h^* and m_e^*, respectively) are plotted as a function of a PBE energy edge descriptor, either E_G^{da} or E_{edge}, depending on which value is higher. Effective masses represents the dispersion of the VB edge (m_h^*) or CB edge (m_e^*) states and are inversely proportional to hole or electron mobility. For the n-type TC screening, we restrict m_e^* to less than 1; however, this tolerance is loosened to m_h^* < 2 for the p-type TC screening to reflect the much smaller distribution of low m_h^* than low m_e^* across materials.[10,28] We restrict our energy screen to compounds with the PBE energy edge descriptor within the range of 1.5–3.2 eV. Note that for transparency in the visible regime, absorption edges greater than 3 eV are desirable; however, PBE can underestimate the band gap by a factor of ~1–2 (depending on chemistry and structure).[29] Hence, the cutoff is reduced by a factor of two. We also include compounds in which the average absorption coefficient $\overline{\alpha}_{vis}$ is less than that of reference compound In_2O_3 (2.7×10^3 cm^{-1} using the PBE functional). In this case, even if a material's absorption edge occurs below 1.5 eV, if its total absorption is low enough, then we still include it in the screen.

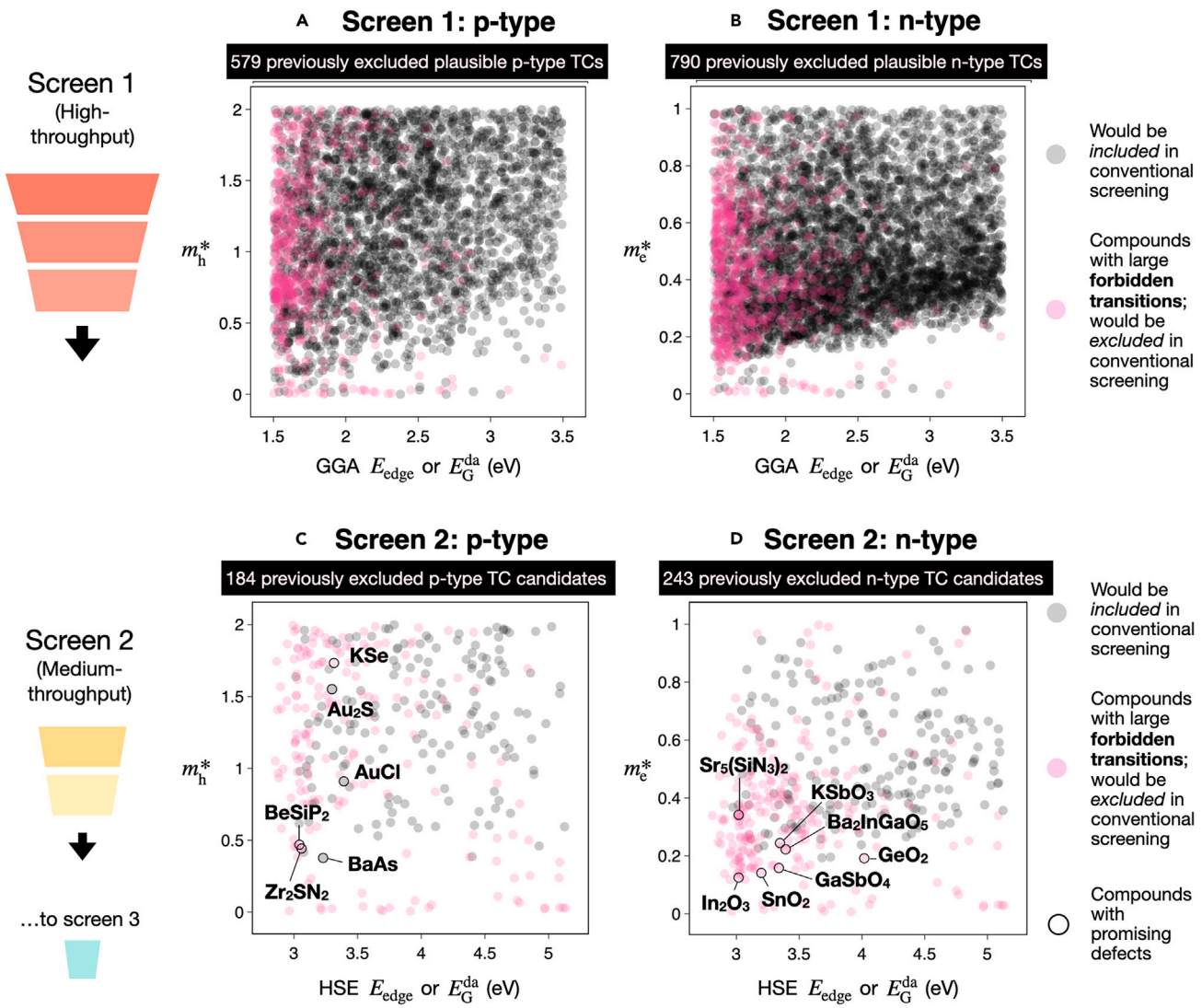

Figure 5. Screening outputs from screen 1 and screen 2

Computed effective mass (m^*) as a function of either E_G^{da} or E_{edge}, depending on which value is higher, to reflect the screening procedure

(A and B) Screen 1 outputs use a PBE functional and energy cutoff of 1.5 eV to reflect PBE's underestimation of energy gap, for (A) plausible p-type TC candidates (focusing on $m_h^* < 2$) and (B) plausible n-type TC candidates (focusing on $m_e^* < 1$).

(C and D) Screen 2 outputs use an HSE functional and energy cutoff of 2.8 eV for (C) p-type TC candidates (focusing on $m_h^* < 2$) and (D) plausible n-type TC candidates (focusing on $m_e^* < 1$). Marker color denotes whether compounds would have been included (blue) or excluded (red) from a conventional screening in which the allowed or forbidden nature of the direct gap is not considered. Candidates emerging from screen 3 are highlighted in (C) and (D).

Figures 5A and 5B plot candidates emerging from screen 1. Pink-colored markers correspond to compounds with large forbidden transitions that would have likely been excluded from previous screens: 579 disperse VB compounds (plausible p-type TCs) and 790 disperse CB compounds (plausible n-type TCs). In total, this amounts to 854 compounds, as most low m_h^* materials also exhibit low m_e^*. Gray-colored markers correspond to other materials within this range with small or no Δ^d, and these amount to 5,209 compounds.

Screen 2: Medium-throughput HSE calculations

In screen 2, band-gap refinement calculations are applied to the outputs of screen 1 to better approximate the direct allowed gap and the absorption coefficient. This

approach assumes that the PBE forbidden energy difference Δ^d is a sufficient proxy for the difference between HSE E_G^d and HSE E_G^{da}; however, this has not been benchmarked to our knowledge, and Δ^d may scale differently depending on the functional. Using these HSE-shifted energies and spectra, compounds are filtered that fulfill at least one of three criteria as proxies for transparency, as shown in Figure 2: $E_G^{da} \geq 2.8$ eV, $E_{edge} \geq 2.8$ eV, or $\overline{\alpha}_{vis}$ less than that of ITO (2.7×10^3 cm^{-1}). Outputs are reported in Figures 5C and 5D, yielding 184 previously excluded p-type TC candidates and 243 previously excluded n-type TC candidates.

At this stage, the branchpoint energy (BPE) ratio σ_{BPE} is also computed as a guideline for whether dopability may be possible. Specifically, BPE energies that lie in the upper quartile of the band gap near the CBM (i.e., $\sigma_{BPE} > 0.75$) have been shown to correlate with unlikely p-type dopability, whereas BPE energies that lie in the lower quartile of the band gap near the VBM (i.e., $\sigma_{BPE} < 0.25$) have been shown to correlate negatively with n-type dopability.[28] Therefore, we restrict defect calculations in screen 3 to compounds with σ_{BPE} <0.75 for p-type candidates and with σ_{BPE} >0.25 for n-type candidates. Most compounds have mid-gap BPEs and so are not excluded from either set. We emphasize that this metric is a guideline that has been demonstrated to correlate with dopability, not to predict it, so screens based on BPE should be used with caution.[28] We have applied BPE to reduce our large dataset to a smaller, computationally tractable subset for lower-throughput screen 3 calculations; however, we acknowledge that we may have screened out false negatives during this step.

Screen 3: Low-throughput defect and mobility calculations

In the final screening step, PBE defect formation energy calculations are performed (with HSE VBM and CBM corrections[30]) to assess accessible intrinsic carrier concentrations on ~100 of the most interesting TC candidates to emerge from screen 2. Many of these compounds have unstable defects (formation energy of the lowest energy defect is less than 0 eV across all Fermi energies) or intrinsic pinning defects such that they are likely not highly dopable (some may be extrinsically dopable, although this has not been investigated here). We identify a subset of compounds with promising dopability, summarized in Table 1 and Figure 6. We will refer to these materials herein as "candidates," as each has shown the potential for dopability, but true dopability remains to be confirmed using higher levels of theory and, for instance, hybrid functionals.

First, our predicted p-type dopable TC candidates include $BeSiP_2$, KSe, Zr_2SN_2, BAs (metastable polymorph with space group $P6_3mc$), Au_2S, and AuCl. All except BAs are on the convex hull and have been synthesized as bulk materials, while the latter two, Au_2S and AuCl, have been synthesized as thin films. Au_2S is a known p-type semiconductor,[32] and the dopability of AuCl is unknown. BAs is a metastable polymorph with space group $P6_3mc$ (its stable cubic polymorph has had recent attention due to its high thermal conductivity,[33,34] and it exhibits p-type conductivity[35]). Compounds $KAlTe_2$, $Cd_3(BO_3)_2$, ScIO, and KCuO are potentially p-type dopable within a smaller window of tolerance. It is noted that previous defect calculations of ScIO suggested pinning near the VBM,[36,37] while KCuO has been proposed previously using the hydrogen descriptor, but defects were not computed. A few p-type candidates appear also n-type dopable at various conditions—$BeSiP_2$, Zr_2SN_2, and KSe (at K_2Se-KSe; see supplemental information)—and therefore may be ambipolar dopable semiconductors; however, in each case, this remains to be confirmed experimentally. We highlight the variety of non-oxide chemistries emerging here; typically forbidden transitions have been studied in oxides, but we demonstrate the importance of looking beyond oxides. In the chalcogenides reported here, p-type dopability is limited by anion vacancies.

Table 1. Most promising predicted TC compounds with forbidden optical transitions (see columns Δ^d and Δ^d_{edge}), and a summary of their computed optical and electronic properties

Material ID (mpid)	Formula	Space group	E_{hull} (eV/at.)[a]	E_G (eV)[a]	E_G (eV)[b]	E_G^d (eV)[b]	E_G^{da} (eV)[c]	E_{edge} (eV)[c]	Δ^d (eV)[a]	Δ^d_{edge} (eV)[c]	$\overline{\alpha}_{vis}$ (cm^{-1})[c]	m_e^*[a]	m_h^*[a]	Doping (defects)[a]	No. ICSD entries
mp-1009085	$BeSiP_2$	$I\bar{4}2d$	0.000	1.15	1.84	1.84	3.04	2.78	1.20	0.94	7.1×10^3	0.35	0.47	p and n	2
mp-9268	KSe	$P\bar{6}2m$	0.000	0.72	1.66	2.14	2.14	3.31	0.00	1.17	4.8×10^3	0.33	1.73	p and n	1
mp-11583	Zr_2SN_2	$P6_3/mmc$	0.000	0.56	1.45	2.65	3.06	2.76	0.41	0.24	8.3×10^3	0.41	0.44	p and n	1
mp-984718	BAs	$P6_3mc$	0.090	1.15	1.82	2.72	3.23	3.05	0.51	0.32	4.6×10^3	0.28	0.38	p-type	0
mp-947	Au_2S	$Pn\bar{3}m$	0.000	1.91	3.00	3.00	3.30	3.14	0.30	0.13	3.4×10^3	0.42	1.55	p-type	2
mp-32780	AuCl	$I4_1/amd$	0.000	1.93	3.04	3.04	3.26	3.39	0.23	0.35	1.9×10^3	1.13	0.91	p-type	2
mp-1072104	GeO_2	$Pnnm$	0.006	1.40	3.23	3.23	3.38	4.02	0.15	0.79	2.2×10^2	0.19	1.62	n-type	6
mp-1224786	$GaSbO_4$	$Cmmm$	0.000	0.80	2.47	2.47	2.83	3.34	0.36	0.87	7.7×10^2	0.16	1.45	n-type	0
mp-16293	$KSbO_3$	$Fd\bar{3}m$	0.045	1.12	2.58	2.89	3.35	3.32	0.46	0.43	1.0×10^3	0.24	0.34	n-type	1
mp-1106089	Ba_2InGaO_5	$Ima2$	0.000	1.42	2.68	2.69	3.27	3.39	0.59	0.71	1.1×10^3	0.22	0.77	n-type	1
mp-1029868	$Sr_5(SiN_3)_2$	$C12/c1$	0.000	1.41	2.43	2.59	2.90	3.02	0.31	0.43	3.7×10^3	0.34	1.20	n-type	0
mp-856	SnO_2	$P4_2/mnm$	0.000	0.66	2.33	2.33	3.06	3.20	0.74	0.87	1.0×10^3	0.14	1.56	n (ref.)	42
mp-22598	In_2O_3	$Ia\bar{3}$	0.000	0.93	2.34	2.34	2.56	3.02	0.22	0.68	2.7×10^3	0.13	6.44	n (ref.)	18

ref., reference. See the supplemental information for full table.
[a]PBE calculations.
[b]HSE06 calculations.
[c]PBE calculations with HSE06 gap correction.

Compounds in which defects suggest candidate n-type TCs include rutile GeO_2, $GaSbO_4$, $KSbO_3$, Ba_2InGaO_5, and $Sr_5(SiN_3)_2$ (as well as ambipolar candidates $BeSiP_2$, KSe, and Zr_2SN_2), while Rb_2SnBr_6, $Sr(YS_2)_2$, and $GaBiO_3$ are potentially n-type dopable within a smaller window of tolerance (see supplemental information). Many of these outputs corroborate literature findings. Notably, the two highest-performing, commercially available n-type TCs—In_2O_3 and SnO_2—emerge from the screening at this stage; both have $\Delta^d > 0$ eV, and we also include them in Table 1 for reference. This is important, as the use of screening parameters from previous studies would have filtered out the best TCs, likely due to their low PBE band gaps (0.66 and 0.93 eV, respectively) and the presence of forbidden transition states at the band edges.[28] Rutile GeO_2 has been recently studied as an ultra-wide-band-gap material and has been shown to be experimentally ambipolar dopable,[38,39] while GeO_2-derived germanates (e.g., $SrGeO_3$) have been explored as n-type TCOs.[40] Sb-based $GaSbO_4$ has been explored preliminarily as an n-type TCO.[41] Perovskite Rb_2SnBr_6 has been recently confirmed experimentally as n-type but has not yet been studied as a TC,[42] while SrY_2S_4 has been grown as a thin film but carrier concentration has not been reported. To our knowledge Ba_2GaInO_5 has been grown in bulk, but not thin-film, form[43] (a similar compound, brownmillerite $Ba_2In_2O_5$, has shown both n-type and p-type doping and ionic conductivity[44]). All oxides in our set are in the main group, corroborating literature consensus on conditions for low effective mass in TCOs[11]; we report several non-oxides here, but in each case, m_e^* is not as high as in oxides.

To assess charge transport, the mobilities of a few representative candidates are computed using the `amset` package.[45] As shown in Figure 7, of these compounds, high hole computed mobilities μ_h (greater than 10 $cm^2V^{-1}s^{-1}$. at 300 K at both moderate and degenerate dopings) are exhibited in $BeSiP_2$, BAs, and Au_2S, with the former two exhibiting $\mu_h > 100$ $cm^2V^{-1}s^{-1}$ $BeSiP_2$ also has a computed electron mobility (μ_e) higher than that of the standards of In_2O_3 and SnO_2, as shown in the supplemental information. Computed mobilities incorporate polar optical phonon, ionized impurity, and acoustic deformation potential scattering modes. These calculations can be interpreted as an upper limit for scattering in high-quality thin films; we do not assess grain-boundary scattering, which is common in thin films.

CellPress

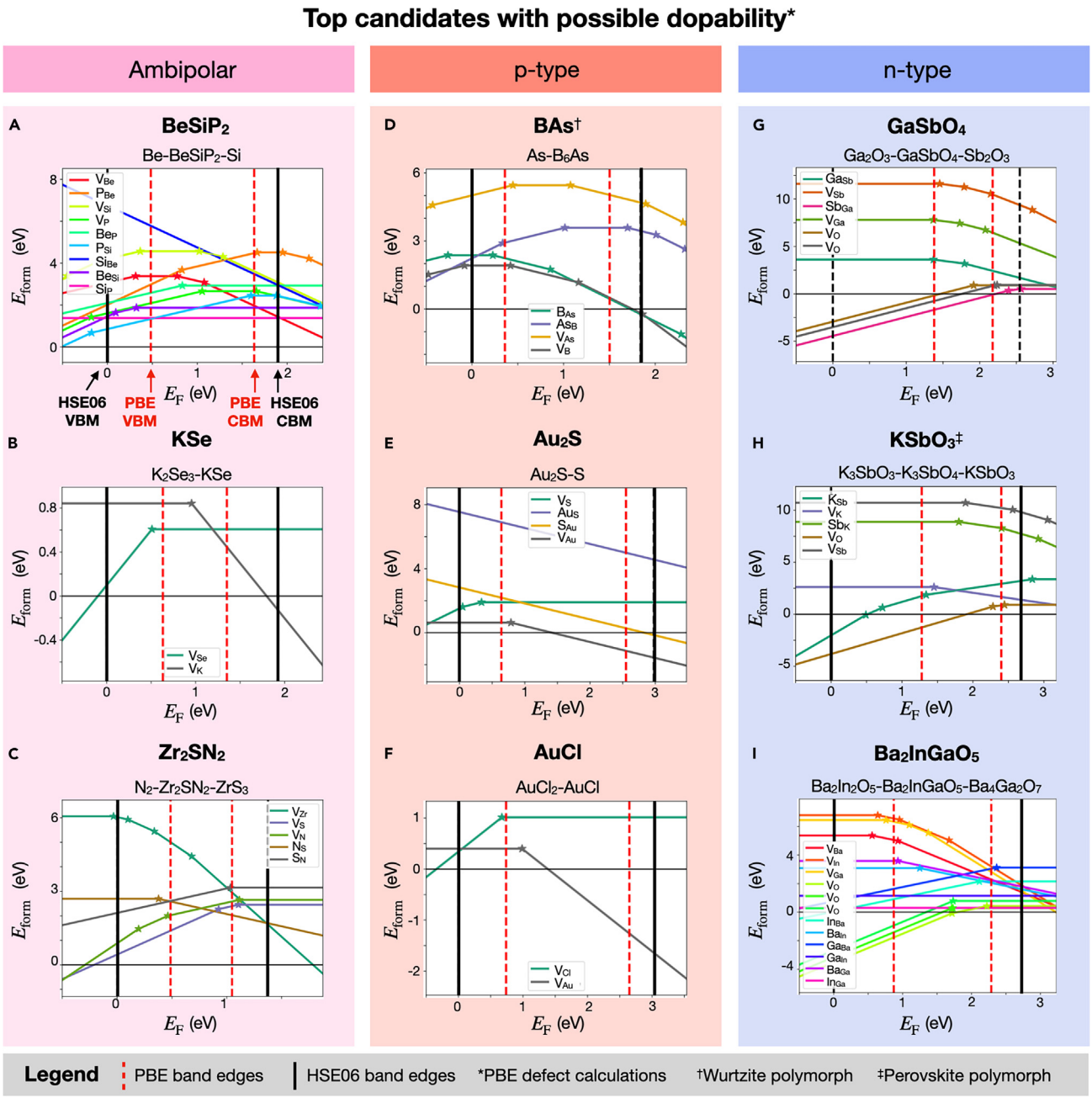

Figure 6. Defect formation energy calculations of top TC screening candidates

(A–I) PBE defect formation energy diagrams for a representative set of (A–C) candidate ambipolar dopable TCs, (D–F) candidate p-type TCs, and (G–I) candidate n-type TCs. Computed chemical potential condition is reported below the compound name and above each subplot, and for each compound only a single representative condition is plotted (see supplemental information for other conditions). The KSe diagram plotted here is for K_2Se_3-KSe and depicts p-type dopability, whereas n-type dopability is computed at a different chemical potential condition (K_2Se-KSe; see supplemental information). We highlight that these are PBE defect calculations (with an HSE band edge "correction"[30]). Doping for $BeSiP_2$ and BAs has been confirmed by higher levels of theory (HSE06) and structural relaxations to account for defect-induced distortions[31] (see supplemental information), but the other compounds in this plot await confirmation of dopability.

To confirm dopability in the two most promising p-type TCs to emerge from the screening—$BeSiP_2$ and BAs—hybrid defect calculations are performed, as summarized in the supplemental information. These calculations corroborate the PBE defect calculations, suggesting (1) ambipolar dopability in $BeSiP_2$, limited by

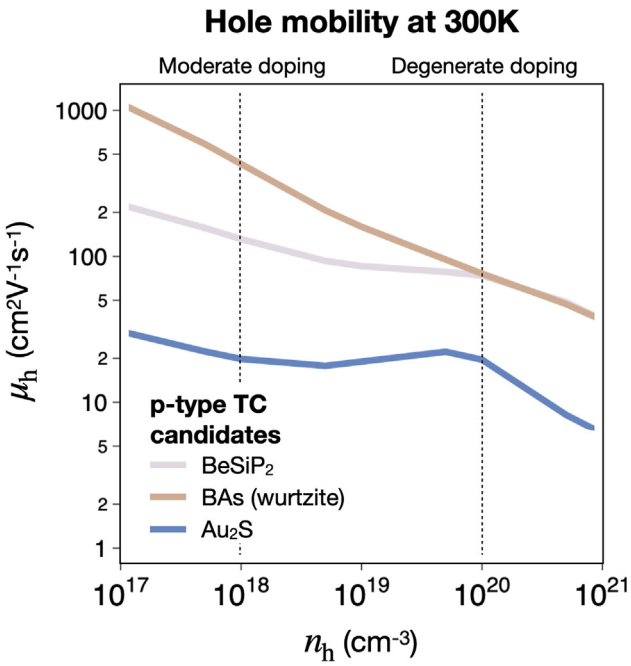

Figure 7. Computed hole mobility of top TC screening candidates

Hole mobility μ_h computed with `amset` code for a representative subset of p-type TC candidates, as a function of doping concentration n_h. See supplemental information for electron mobility calculations.

phosphorus vacancies (V_P) for p-type doping and beryllium vacancies (V_{Be}) for n-type doping, and (2) p-type dopability BAs, limited by boron vacancies (V_B).

Identification of candidate TCs with forbidden transitions

Here, we summarize the optical and electronic properties of the most promising candidates to emerge from GGA defect calculations, as reported in Table 1, and highlight a few examples. Each emerging compound has a GGA gap E_G below 2 eV, but either an HSE-corrected E_G^{da} or E_{edge} greater than 3 eV due to the presence of forbidden transitions or a high Δ^d_{edge}. Au_2S, AuCl, and GeO_2 have HSE gaps E_G greater than 3 eV and so may have emerged from previous screenings but are included here due to their forbidden transitions; KSe does not have forbidden transitions, but Δ^d_{edge} is greater than 1 eV, so it is included as well. Compounds in which $\overline{\alpha}_{vis}$ is less than that of In_2O_3 and likely exhibit a high degree of transparency are GeO_2, AuCl, $KSbO_3$, and Ba_2InGaO_5. The former has been investigated in depth, but the latter three would be particularly interesting candidates for follow-up studies.

In Figure 8, we highlight (Figures 8A–8Cc) crystal structure and (Figures 8D–DL) optical properties for candidates chalcopyrite $BeSiP_2$ and wurtzite BAs, selected as representative materials since charge transport and hybrid defect calculations have confirmed p-type dopability and mobility, as well as predicted brownmillerite Ba_2InGaO_5 as an n-type TC example. The electronic band-structure diagrams of $BeSiP_2$ (Figure 8D), BAs (Figure 8E), and Ba_2InGaO_5 (Figure 8F) demonstrate that the direct allowed gap E_G^{da} (pink arrow) is larger than E_G^d (black arrow) and that the band extrema at Γ are very disperse, which leads to low effective masses and high mobilities. The gray shading depicts regions in which optical transitions are forbidden. For example, in Ba_2InGaO_5 (Figure 8F), transitions between the upper

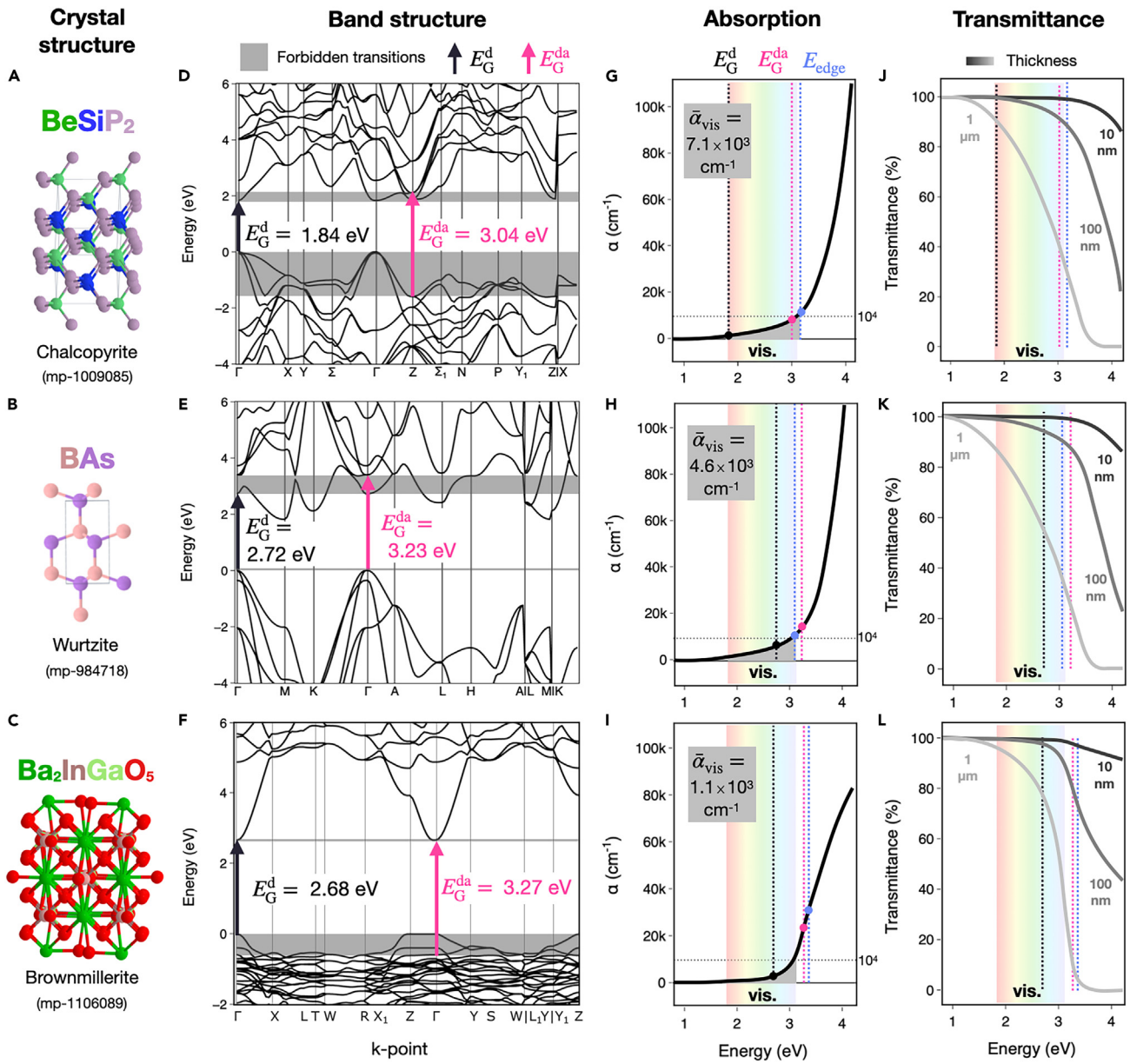

Figure 8. Structural and optical properties of top TC screening candidates

(A–L) (A–C) Crystal structure, (D–F) HSE-corrected electronic band diagram, (G–I) computed absorption coefficient, and (J–L) computed transmittance for three representative candidates from our screening with forbidden optical transitions: ambipolar-dopable $BeSiP_2$, p-type dopable BAs, and n-type dopable Ba_2InGaO_5. HSE direct and direct allowed gaps E_G^d and E_G^{da} are denoted with black and pink lines, respectively, and in (D)–(F), gray shading indicates the region in which optical transitions are forbidden between the VB and CB states. Rainbow shading in (J)–(L) corresponds the visible spectrum ("vis."), and line color is the thickness of a simulated thin film (assuming negligible reflectance).

two VBs along the Γ-X, Γ-Y, and Γ-Z paths, as well as the L-T-W path, are forbidden. Thus, the third-highest VB is the highest VB at which transitions between the CBM are allowed, and $E_G^{da,HSE}$ occurs at the Γ point at approximately −0.6 eV. These examples demonstrate three different scenarios in which forbidden transitions can occur. In Ba_2InGaO_5 the E_G^{da} and E_G^d occur at the same k-point (Γ), and states are forbidden at the VBM; in BAs, the E_G^{da} and E_G^d occur at the same k-point (Γ), and states are forbidden at the CBM, while in $BeSiP_2$, E_G^{da} occurs at a different k-point (Z) than E_G^d (Γ), and states are forbidden both at the VBM and the CBM.

Panels (Figures 8G–8I) show HSE-corrected absorption coefficient as a function of photon energy, with the edge energy difference E_{edge} denoted. In each example material, the E_{edge} is within a few tens of meV of the E_G^{da}, although in other candidates, this is not necessarily the case (see Table 1, e.g., In_2O_3). Importantly, in both cases, E_{edge} is at the violet edge of the visible spectrum, which indicates a likelihood of transparency in the visible. Figures 8J and 8K) report transmittance from the Beer-Lambert law (see supplemental information), and the color of the trace corresponds to the thickness of a thin film. As expected, thinner films are more transparent; however, the decrease in transparency as thickness increases is material dependent. For example, although both $BeSiP_2$ and Ba_2InGaO_5 have >99% transmittance for 10-nm-thick films, 1-μm-thick films of Ba_2InGaO_5 have a T_{vis} of ~75%, while T_{vis} drops to less than 50% in $BeSiP_2$. However, although $BeSiP_2$ has >99% transmittance for 10-nm-thick films, T_{vis} drops to less than 50% in 1-μm-thick films. Therefore, this metric is important when selecting materials for real device applications.

DISCUSSION

Synthesis considerations

So far, we have used simulations to predict properties; the next step for the TC community is to synthesize these materials as thin films and assess their properties experimentally. The final column of Table 1 reports the number of experimental ICSD database entries, showing that all but three (BAs, $Sr_5(SiN_3)_2$, $GaSbO_4$) have been previously synthesized (although $GaSbO_4$ has been recently reported[41]). However, in many compounds with ICSD entries, thin films have not yet been grown nor characterized, and dopabilty has not been assessed experimentally (e.g., $BeSiP_2$, KSe, Ba_2InGaO_5, Zr_2SN_2, etc.).

Some of our candidates have known synthesis challenges, in particular since thin-film synthesis is often at non-equilibrium conditions and presents other difficulties. In perovskite oxides $KSbO_3$ and $GaBiO_3$, low m_e^* has been highlighted,[11] but phase-pure thin-film synthesis has proven challenging, so doping remains to be confirmed.[46] Non-oxide chalcogenides yield particular synthesis barriers due to moisture- or air-induced decomposition: for example, KSe has not been synthesized as a thin film to our knowledge. For candidates that do not have ICSD entries or recent experimental reports, synthesis may have been attempted but was not successful for various reasons. Wurtzite BAs has been challenging to crystallize and has not yet been synthesized as a thin film to our knowledge; it is similar in chemistry to zinc blende BP, which was predicted computationally as a p-type TC[19] and has since been synthesized as a thin film.[47]

We acknowledge that some of these candidates are also likely not practical or safe to scale up into device applications. In particular, Be and Be-containing compounds are toxic to humans and the environment,[48] so although $BeSiP_2$ has been synthesized, it is most likely not a practical TC material. However, since this compound has a common chalcopyrite crystal structure with a small unit cell, its combination of large forbidden transitions and a disperse VB is demonstrative and could inspire design criteria of other p-type TCs (see Figure 8).

Challenges and open questions

From the set of 18,000 materials with absorption calculations, we have proposed a set of TC candidates with forbidden optical transitions at their band edges and with plausible dopability and high mobility. There is a general correlation across all semiconductors that as the fundamental electronic gap increases, doping becomes more

challenging, and band edges become less disperse.[49,50] Previous searches for p-type TCs have endeavored to identify cases in which a single state at the VBM is both disperse over k-space and facilitates transitions that lead to a wide gap. In contrast, by decoupling these two parameters such that allowed transitions do not need to occur at the band edge, our metric could enable better electronic properties while the optical gap is widened.

One challenge with this design metric is that localized band edges, which we have shown to correlate with forbidden transitions, tend to lead to higher effective masses and therefore lower mobilities. However, we have demonstrated that ~90% of materials with forbidden transitions have at least one delocalized band edge. Notably, in all of the proposed low effective mass TC candidates in Table 1 with Δ^d >0 eV, including the most promising candidates $BeSiP_2$ and wurtzite BAs, forbidden transitions at the band edges occur between two delocalized states (D $\rightarrow D$) rather than between localized states (see supplemental information). Therefore, in our TC candidates and in the majority of our identified semiconductors with forbidden transitions, the origin of the forbidden nature has not yet been identified and remains an open question.

The absorption spectra we have computed are first-order, high-throughput approximations, and therefore interpretation of results must consider their limitations. IPA calculations account only for interband absorption at a fixed k-point and do not consider intraband absorption matrix elements, and additional contributions from indirect transitions are excluded. Our calculations may be sufficient for a first-order approximation since indirect absorption tends to be weak, but in heavily doped TCs, strong free-carrier absorption can arise due to intraband transitions.[51] We do not include the effects of electron-hole interactions or spin-orbit coupling, which may influence the orbital character of the band edges or induce spin-forbidden transitions.

Off stoichiometries and dopants can also introduce shallow defect levels within the gap that reduce optical transparency, and absorption from excitons may also become significant at energies just below the fundamental absorption edge, leading to a reduction of transparency.[51] On the contrary, high doping can lead to the Moss-Burstein effect and a widening of the gap.[52,53] Perhaps Moss-Burstein shifts could be combined with the widening from forbidden transitions as another route to designing TCs, though this has not been explored in this study. Additionally, to maintain a computationally tractable dataset, we have not explored materials with PBE gaps in the range 0 eV < E_G < 0.5 eV, but it is possible that some materials in this regime may also exhibit large forbidden transitions. Despite these limitations, our calculations and data have added information and improved design metrics toward furthering the search for novel TCs.

Conclusion

In this study, we have described the absorption edge and OT for ~18,000 semiconductors in the MP database, and we have shared these data publicly on the MPContribs platform. Using a set of descriptors for absorption and orbital character, we have demonstrated correlations between the presence of forbidden optical transitions, localized band edges, and orbital similarity. However, a mechanistic explanation of the origin of forbidden transitions across materials with delocalized band edges remains an open question. From this set of materials, we have screened for n-type or p-type TCs, and propose a set of candidates with forbidden band-edge transitions and promising optical and electronic properties such as chalcopyrite

$BeSiP_2$ and wurtzite BAs. Notably, high-performance TCs such as ITO emerge from this screening, while they would have been excluded from screenings based on the fundamental gap alone. Since over half of the set of ~18,000 semiconductors have forbidden optical transitions at their band edges (OT2 or OT4), we recommend that future high-throughput screenings for optical properties use metrics representative of absorption spectra rather than band gap alone.

EXPERIMENTAL PROCEDURES

Resource availability

Lead contact

Further information and requests for resources should be directed to and will be fulfilled by the lead contact, Rachel Woods-Robinson (rwoodsrobinson@berkeley.edu).

Materials availability

No new materials were generated for this study.

Data and code availability

All tabulated properties will be uploaded to the MPContribs platform at https://doi.org/10.17188/mpcontribs/1996545 and will be available free of charge. All data needed to evaluate the conclusions in the paper are present in the paper and/or the supplemental information.

Method details

DFT calculations were performed using the projector augmented wave (PAW) method[54,55] as implemented in the Vienna *Ab Initio* Simulation Package (VASP),[56,57] first within the PBE GGA formulation of the exchange-correlation functional.[58] Cutoff, convergence, and correction criteria have been benchmarked and are used throughout the MP infrastructure, as described elsewhere.[59,60] m^* was computed from GGA calculations using the `BoltzTraP2` package,[61] assuming dopings of 10^{18} cm^{-3} as described in the supplemental information. The HSE06-screened hybrid functional[62] was used to calculate gap corrections and apply scissor shifts in screen 2. BPE was computed from GGA calculations with an HSE gap correction; the BPE ratio range σ_{BPE} was computed by varying numbers of VBs (N_{VB}) and numbers of CBs (N_{CB}) from N_{VB}: N_{CB} = 2:4 to N_{CB}: N_{CB} = 8:4, with details described elsewhere.[28] The site-projected wave function character of orbitals at the band edges were assessed to compute the IPRs and the orbital similarities (see supplemental information).

Optical absorption coefficients were calculated with VASP using the Independent Particle Approximation (IPA). Using the IPA, the dielectric matrix elements are calculated using a k-point reciprocal density of 1,000 $Å^{-3}$, which we have benchmarked and optimized for high-throughput screenings of E_{edge} (for optimization of precision in the extended absorption spectrum, see Yang et al.[63]). Cutoff for a transition to be considered allowed was selected following convention from Fabini et al.[21] Details and calculation parameters for this method are reported in the supplemental information.

Focusing on compounds that are likely to be synthesizable and are tractable for further defect calculations, we pre-screen (see Figure 2) the MP database using a series of filters. We include compounds in which the MP computed GGA fundamental band gap (E_G) is greater than 0.5 eV and the energy above convex hull (E_{hull}) is less than 0.1 eV/atom.[64,65] Large compounds were filtered out with more than 5 elements or more than 12 symmetrically inequivalent sites (see `pymatgen.symmetry.analyzer`). Compounds with heavy elements (Z > 82) and f-block

elements are also filtered out (except for La). GGA absorption spectra of ~800 MP compounds from Fabini et al.'s search for photovoltaic absorber materials are publicly available on MPContribs and are included in our set.[21,66]

For compounds that emerge from screen 2, defect formation energy calculations are performed using the `pycdt` package,.[67] Hybrid DFT calculations of defect formation energies are performed using the CP2K software package and HSE06 functional.[62,68,69] Charge-carrier mobility is calculated using the *ab initio* scattering and transport package (`amset`),[45] which solves the linearized Boltzmann transport equation under the constant relaxation time approximation. Details for each of these methods are described in the supplemental information.

SUPPLEMENTAL INFORMATION

Supplemental information can be found online at https://doi.org/10.1016/j.matt.2023.06.043.

ACKNOWLEDGMENTS

We thank Doug Fabini for helpful discussions and Ruoxi Yang, Jason Munro, and David Mrdjenovich for fruitful discussion and insights. This work was supported by the US Department of Energy, Office of Science, Office of Basic Energy Sciences, Materials Sciences and Engineering Division, under contract no. DE-AC02-05-CH11231 (Materials Project program KC23MP). R.W.-R. was supported by the U.C. Berkeley Chancellor's Fellowship and the National Science Foundation (NSF) Graduate Research Fellowship under grant nos. DGE1106400 and DGE175814. A.M.G. was supported by EPSRC Fellowship EP/T033231/1. We acknowledge compute resources from National Energy Research Scientific Computing Center (NERSC), a DOE Office of Science User Facility.

AUTHOR CONTRIBUTIONS

Conceptualization, R.W.-R. and G.H.; methodology, R.W.-R. and M.K.S.; coding, R.W.-R., J.-X.S., and M.K.S.; computational investigation, R.W.-R., Y.X. (PBE defect formation energy calculations), N.W. (HSE defect formation energy calculations), and A.M.G. (amset calculations); writing – original draft, R.W.-R.; writing – review & editing, R.W.-R., G.H., and K.A.P.; funding acquisition, R.W.-R., M.A., and K.A.P.; supervision, J.-X.S., M.K.S., M.A., G.H., and K.A.P.; resources, M.A. and K.A.P.; project administration, K.A.P.

DECLARATION OF INTERESTS

The authors declare no competing interests.

Received: April 19, 2023
Revised: June 19, 2023
Accepted: June 28, 2023
Published: September 6, 2023

REFERENCES

1. Yu, L., and Zunger, A. (2012). Identification of potential photovoltaic absorbers based on first-principles spectroscopic screening of materials. Phys. Rev. Lett. *108*, 068701.
2. Böer, K.W., and Pohl, U.W. (2023). Semiconductor Physics (Springer Nature).
3. Walsh, A., Da Silva, J.L.F., Wei, S.-H., Körber, C., Klein, A., Piper, L.F.J., DeMasi, A., Smith, K.E., Panaccione, G., Torelli, P., et al. (2008). Nature of the band gap of In_2O_3 revealed by first-principles calculations and x-ray spectroscopy. Phys. Rev. Lett. *100*, 167402.
4. Summitt, R., Marley, J.A., and Borrelli, N.F. (1964). The ultraviolet absorption edge of stannic oxide (SnO_2). J. Phys. Chem. Solid. *25*, 1465–1469.
5. Fröhlich, D., Kenklies, R., and Helbig, R. (1978). Band-gap assignment in SnO_2 by

two-photon spectroscopy. Phys. Rev. Lett. *41*, 1750–1751.

6. Segev, D., and Wei, S.-H. (2005). Structure-derived electronic and optical properties of transparent conducting oxides. Phys. Rev. B *71*, 125129.

7. Kehoe, A.B., Scanlon, D.O., and Watson, G.W. (2011). Nature of the band gap of Tl_2O_3. Phys. Rev. B *83*, 233202.

8. Tang, H., Berger, H., Schmid, P., and Lévy, F. (1994). Optical properties of anatase (Tl_2O_3). Solid State Commun. *92*, 267–271.

9. Nie, X., Wei, S.-H., and Zhang, S.B. (2002). Bipolar doping and band-gap anomalies in delafossite transparent conductive oxides. Phys. Rev. Lett. *88*, 066405.

10. Hautier, G., Miglio, A., Ceder, G., Rignanese, G.-M., and Gonze, X. (2013). Identification and design principles of low hole effective mass p-type transparent conducting oxides. Nat. Commun. *4*, 2292.

11. Hautier, G., Miglio, A., Waroquiers, D., Rignanese, G.-M., and Gonze, X. (2014). How does chemistry influence electron effective mass in oxides? a high-throughput computational analysis. Chem. Mater. *26*, 5447–5458.

12. Bhatia, U., Hautier, G., Nilgianskul, T., Miglio, A., Sun, J., Kim, H.J., Kim, K.H., Chen, S., Rignanese, G.-M., Gonze, X., and Suntivich, J. (2015). High-mobility bismuth-based transparent p-type oxide from high-throughput material screening. MLO. Med. Lab. Obs. *47*, 30–34.

13. Ha, V.-A., Yu, G., Ricci, F.R., Diana, D., Setten, M.J.V., Giantomassi, M., Rignanese, G.-M., and Hautier, G. (2018). Computationally-driven, high throughput identification of CaTe and Li_3Sb as promising candidates for high mobility p-Type transparent conducting materials. Manuscript in preparation *3*, 34601.

14. Brunin, G., Ricci, F., Ha, V.-A., Rignanese, G.-M., and Hautier, G. (2019). Transparent conducting materials discovery using high-throughput computing. npj Comput. Mater. *5*, 63.

15. Jackson, A.J., Parrett, B.J., Willis, J., Ganose, A.M., Leung, W.W.W., Liu, Y., Williamson, B.A.D., Kim, T.K., Hoesch, M., Veiga, L.S.I., et al. (2022). Computational prediction and experimental realization of earth-abundant transparent conducting oxide Ga-doped $ZnSb_2O_6$. ACS Energy Lett. *7*, 3807–3816.

16. Sarmadian, N., Saniz, R., Partoens, B., and Lamoen, D. (2016). Easily doped p-type, low hole effective mass, transparent oxides. Sci. Rep. *6*, 20446.

17. Williamson, B.A.D., Buckeridge, J., Brown, J., Ansbro, S., Palgrave, R.G., and Scanlon, D.O. (2016). Engineering valence band dispersion for high mobility p-type semiconductors. Chem. Mater. *29*, 2402–2413.

18. Shi, J., Cerqueira, T.F.T., Cui, W., Nogueira, F., Botti, S., and Marques, M.A.L. (2017). High-throughput search of ternary chalcogenides for p-Type transparent electrodes. Sci. Rep. *7*, 43179.

19. Varley, J.B., Miglio, A., Ha, V.A., van Setten, M.J., Rignanese, G.M., and Hautier, G. (2017). High-throughput design of non-oxide p-type transparent conducting materials: Data mining, search strategy, and identification of boron phosphide. Chem. Mater. *29*, 2568–2573.

20. Meng, W., Wang, X., Xiao, Z., Wang, J., Mitzi, D.B., and Yan, Y. (2017). Parity-forbidden transitions and their impact on the optical absorption properties of lead-free metal halide perovskites and double perovskites. J. Phys. Chem. Lett. *8*, 2999–3007.

21. Fabini, D.H., Koerner, M., and Seshadri, R. (2019). Candiyear inorganic photovoltaic materials from electronic structure-based optical absorption and charge transport proxies. Chem. Mater. *31*, 1561–1574.

22. Morales-García, Á., Valero, R., and Illas, F. (2017). An empirical, yet practical way to predict the band gap in solids by using density functional band structure calculations. J. Phys. Chem. C *121*, 18862–18866.

23. Yu, P.Y., and Cardona, M. (2005). Fundamentals of Semiconductors, 4 ed. (Elsevier).

24. Wegner, F. (1980). Inverse participation ratio in 2+ ε dimensions. Z. Physik B *36*, 209–214.

25. Pashartis, C., and Rubel, O. (2017). Localization of electronic states in III-V semiconductor alloys: A comparative study. Phys. Rev. Applied *7*, 064011.

26. Konstantinou, K., Mocanu, F.C., Lee, T.-H., and Elliott, S.R. (2019). Revealing the intrinsic nature of the mid-gap defects in amorphous $Ge_2Sb_2Te_5$. Nat. Commun. *10*, 3065.

27. Xiong, Y., Bourgois, C., Sheremetyeva, N., Chen, W., Dahliah, D., Song, H., Griffin, S.M., Sipahigil, A., and Hautier, G. (2023). High-throughput identification of spin-photon interfaces in silicon. Preprint at arXiv. https://doi.org/10.48550/arXiv.2303.01594.

28. Woods-Robinson, R., Broberg, D., Faghaninia, A., Jain, A., Dwaraknath, S.S., and Persson, K.A. (2018). Assessing high-throughput descriptors for prediction of transparent conductors. Chem. Mater. *30*, 8375–8389.

29. Chan, M.K.Y., and Ceder, G. (2010). Efficient band gap prediction for solids. Phys. Rev. Lett. *105*, 196403.

30. Broberg, D., Bystrom, K., Srivastava, S., Dahliah, D., Williamson, B.A.D., Weston, L., Scanlon, D.O., Rignanese, G.-M., Dwaraknath, S., Varley, J., et al. (2023). High-throughput calculations of charged point defect properties with semi-local density functional theory - performance benchmarks for materials screening applications. npj Comput. Mater.

31. Mosquera-Lois, I., Kavanagh, S.R., Walsh, A., and Scanlon, D.O. (2023). Identifying the ground state structures of point defects in solids. npj Comput. Mater. *9*, 25.

32. Ishikawa, K., Isonaga, T., Wakita, S., and Suzuki, Y. (1995). Structure and electrical properties of Au_2S. Solid State Ionics *79*, 60–66.

33. Lindsay, L., Broido, D.A., and Reinecke, T.L. (2013). First-principles determination of ultrahigh thermal conductivity of boron arsenide: A competitor for diamond? Phys. Rev. Lett. *111*, 025901.

34. Kang, J.S., Li, M., Wu, H., Nguyen, H., and Hu, Y. (2018). Experimental observation of high thermal conductivity in boron arsenide. Science *361*, 575–578.

35. Lyons, J.L., Varley, J.B., Glaser, E.R., Freitas, J.A., Jr., Culbertson, J.C., Tian, F., Gamage, G.A., Sun, H., Ziyaee, H., and Ren, Z. (2018). Impurity-derived p-type conductivity in cubic boron arsenide. Appl. Phys. Lett. *113*, 251902.

36. Yim, K., Youn, Y., Lee, M., et al. (2018). Computational discovery of p-type transparent oxide semiconductors using hydrogen descriptor. npj Comput Mater *4*, 17.

37. Wiebeler, H., Raghupathy, R.K.M., Mirhosseini, H., and D Kühne, T. (2020). Virtual screening of nitrogen-phosphorous-and halide-containing materials as p-type transparent conductors. J. Phys. Mater. *4*, 015004.

38. Chae, S., Lee, J., Mengle, K.A., Heron, J.T., and Kioupakis, E. (2019). Rutile GeO2: an ultrawide-band-gap semiconductor with ambipolar doping. Appl. Phys. Lett. *114*, 102104.

39. Chae, S., Mengle, K., Bushick, K., Lee, J., Sanders, N., Deng, Z., Mi, Z., Poudeu, P.F., Paik, H., Heron, J.T., et al. (2021). Toward the predictive discovery of ambipolarly dopable ultra-wide-band-gap semiconductors: The case of rutile GeO2. Appl. Phys. Lett. *118*, 260501.

40. Mizoguchi, H., Kamiya, T., Matsuishi, S., and Hosono, H. (2011). A germanate transparent conductive oxide. Nat. Commun. *2*, 470.

41. Leung, W.W. (2020). Synthesis and Characterisation of Group 15-containing Inorganic Solids for Energy Conversion Applications (UCL (University College London)).

42. Ganesan, R., Vinodhini, S.P., Arulmozhi, R., and Muralidharan, R. (2023). Influence of halogen substitution in double perovskite $Rb_2Sn(Br_{0.75}I_{0.25})_6$ on the photocatalytic degradation of methylene blue dye under visible light irradiation. J. Mater. Sci. Mater. Electron. *34*, 151.

43. Didier, C., Claridge, J., and Rosseinsky, M. (2014). Crystal structure of brownmillerite Ba_2InGaO_5. J. Solid State Chem. *218*, 38–43.

44. Fisher, C., and Islam, M. (1999). Defect, protons and conductivity in brownmillerite-structured $Ba_2In_2O_5$. Solid State Ionics *118*, 355–363.

45. Ganose, A.M., Park, J., Faghaninia, A., Woods-Robinson, R., Persson, K.A., and Jain, A. (2021). Efficient calculation of carrier scattering rates from first principles. Nat. Commun. *12*, 2222.

46. Homcheunjit, R., Pluengphon, P., Tubtimtae, A., and Teesetsopon, P. (2022). Structural, optical, and electrical properties via two simple routes for the synthesis of multi-phase potassium antimony oxide thin films. Phys. B Condens. Matter *637*, 413885.

47. Crovetto, A., Adamczyk, J.M., Schnepf, R.R., Perkins, C.L., Hempel, H., Bauers, S.R., Toberer, E.S., Tamboli, A.C., Unold, T., and Zakutayev, A. (2022). Boron phosphide films by reactive sputtering: Searching for a p-type transparent conductor. Adv. Mater. Interfaces *9*, 2200031.

48. Smith, C., Ingerman, L., and Amata, R. (2002). Toxicological Profile for Beryllium.

49. Zunger, A. (2003). Practical doping principles. Appl. Phys. Lett. *83*, 57–59.

50. Kittel, C., and Kittel, B. (1986). Introduction to Solid State Physics, *8* (Wiley).

51. Pankove, J.I. (1975). Optical Processes in Semiconductors (Courier Corporation).

52. Burstein, E. (1954). Anomalous optical absorption limit in InSb. Phys. Rev. *93*, 632–633.

53. Moss, T.S. (1954). The interpretation of the properties of indium antimonide. Proc. Phys. Soc. B *67*, 775–782.

54. Blöchl, P.E. (1994). Projector augmented-wave method. Phys. Rev. B *50*, 17953–17979.

55. Kresse, G., and Joubert, D. (1999). From ultrasoft pseudopotentials to the projector augmented-wave method. Phys. Rev. B *59*, 1758–1775.

56. Kresse, G., and Hafner, J. (1993). *Ab initio* molecular dynamics for liquid metals. Phys. Rev. B *47*, 558–561.

57. Kresse, G., and Furthmüller, J. (1996). Efficient iterative schemes for *Ab initio* total-energy calculations using a plane-wave basis set. Phys. Rev. B *54*, 11169–11186.

58. Perdew, J.P., Burke, K., and Ernzerhof, M. (1996). Generalized gradient approximation made simple. Phys. Rev. Lett. *77*, 3865–3868.

59. Ong, S.P., Richards, W.D., Jain, A., Hautier, G., Kocher, M., Cholia, S., Gunter, D., Chevrier, V.L., Persson, K.A., and Ceder, G. (2013). Python materials genomics (pymatgen): A robust, open-source python library for materials analysis. Comput. Mater. Sci. *68*, 314–319.

60. Jain, A., Ong, S.P., Hautier, G., Chen, W., Richards, W.D., Dacek, S., Cholia, S., Gunter, D., Skinner, D., Ceder, G., and Persson, K.A. (2013). Commentary: The Materials Project: A materials genome approach to accelerating materials innovation. Apl. Mater. *1*, 011002.

61. Madsen, G.K., Carrete, J., and Verstraete, M.J. (2018). Boltztrap2, a program for interpolating band structures and calculating semi-classical transport coefficients. Comput. Phys. Commun. *231*, 140–145.

62. Heyd, J., Scuseria, G.E., and Ernzerhof, M. (2003). Hybrid functionals based on a screened coulomb potential. J. Chem. Phys. *118*, 8207–8215.

63. Yang, R.X., Horton, M.K., Munro, J., and Persson, K.A. (2022). High-throughput optical absorption spectra for inorganic semiconductors. Preprint at arXiv. https://doi.org/10.48550/arXiv.2209.02918.

64. Aykol, M., Dwaraknath, S.S., Sun, W., and Persson, K.A. (2018). Thermodynamic limit for synthesis of metastable inorganic materials. Sci. Adv. *4*, eaaq0148.

65. Sun, W., Dacek, S.T., Ong, S.P., Hautier, G., Jain, A., Richards, W.D., Gamst, A.C., Persson, K.A., and Ceder, G. (2016). The thermodynamic scale of inorganic crystalline metastability. Sci. Adv. *2*, e1600225.

66. Huck, P., Gunter, D., Cholia, S., Winston, D., N'Diaye, A., and Persson, K. (2016). User applications driven by the community contribution framework mpcontribs in the materials project. Concurrency Computat, Pract. Exper. *28*, 1982–1993.

67. Broberg, D., Medasani, B., Zimmermann, N.E., Yu, G., Canning, A., Haranczyk, M., Asta, M., and Hautier, G. (2018). Pycdt: A python toolkit for modeling point defects in semiconductors and insulators. Comput. Phys. Commun. *226*, 165–179.

68. Hutter, J., Iannuzzi, M., Schiffmann, F., and VandeVondele, J. (2014). Cp2k: atomistic simulations of condensed matter systems. WIREs. Comput. Mol. Sci. *4*, 15–25.

69. Kühne, T.D., Iannuzzi, M., Del Ben, M., Rybkin, V.V., Seewald, P., Stein, F., Laino, T., Khaliullin, R.Z., Schütt, O., Schiffmann, F., et al. (2020). Cp2k: An electronic structure and molecular dynamics software package-quickstep: Efficient and accurate electronic structure calculations. J. Chem. Phys. *152*, 194103.